Eur. Phys. J. B **54**, 471–477 (2006)
DOI: 10.1140/epjb/e2007-00027-5

THE EUROPEAN PHYSICAL JOURNAL B

Shape dependent electronic structure and exciton dynamics in small In(Ga)As quantum dots

J. Gomis[1,a], J. Martínez-Pastor[1], B. Alén[1], D. Granados[2], J.M. García[2], and P. Roussignol[3]

[1] Institut de Ciències dels Materials, Universitat de València, P.O. Box 22085, 46071 València, Spain
[2] Instituto de Microelectrónica de Madrid (CNM-CSIC), Isaac Newton 8, 28760 Tres Cantos, Madrid, Spain
[3] Laboratoire Pierre Aigrain, École Normale Supérieure, 24 rue Lhomond, 75231 Paris Cedex 05, France

Received 25 September 2006 / Received in final form 1st December 2006
Published online 3 February 2007 – © EDP Sciences, Società Italiana di Fisica, Springer-Verlag 2007

Abstract. We present a study of the primary optical transitions and recombination dynamics in InGaAs self-assembled quantum nanostructures with different shape. Starting from the same quantum dot seeding layer, and depending on the overgrowth conditions, these new nanostructures can be tailored in shape and are characterized by heights lower than 2 nm and base lengths around 100 nm. The geometrical shape strongly influences the electronic and optical properties of these nanostructuctures. We measure for them ground state optical transitions in the range 1.25–1.35 eV and varying energy splitting between their excited states. The temperature dependence of the exciton recombination dynamics is reported focusing on the intermediate temperature regime (before thermal escape begins to be important). In this range, an important increase of the effective photoluminescence decay time is observed and attributed to the state filling and exciton thermalization between excited and ground states. A rate equation model is also developed reproducing quite well the observed exciton dynamics.

PACS. 78.67.Hc Quantum dots – 73.21.La Quantum dots – 78.55.Cr III-V semiconductors

1 Introduction

Due to the noticeable reduction of the laser diode threshold current, in the last years, quantum dots (QDs) are substituting quantum wells into laser diode active layers even if good size uniformity and tuning of the emission wavelength in a continuous way are difficult to achieve [1]. Typical InAs/GaAs self-assembled QD emission takes place around 1.12 μm at room temperature. Therefore, to extend their application range to the spectral windows of interest around 1.5 μm, the most common strategies are based in the use of the InGaAs [2] or GaAsSb [3] alloys, for either the dot or the dot capping layers. Similar efforts have been devoted to extend the emission towards lower wavelengths and, some years ago, "quantum ring" (QR) structures were obtained emitting at 0.98 μm at room temperature [4]. These ring-shaped nanostructures were obtained by a self-assembled process overgrowing specially high pyramidal QDs under suitable growth conditions [5]. Now, this growth technique is better understood and different shape nanostructures can be obtained with different vertical and lateral confinement potentials. On the one hand, the strong vertical confinement determines the blueshift of the ground state emission compared with standard InAs/GaAs QDs. On the other hand, the lateral potential is the main responsible for the energy separation between ground and excited states [6], and plays an important role in the room temperature performance of optoelectronic devices based on these nanostructures. In this work, we will study some basic optical properties of such a kind of different shape QDs, mainly those related to their electronic structure and exciton recombination dynamics at low and high temperatures.

2 Samples and experiment

The three samples studied in this work follow a similar growth procedure. An initial QD seeding layer is grown by depositing 1.7 monolayers (ML) of InAs onto a (001)-GaAs substrate (after a GaAs buffer layer) at 540 °C, under an As_2 beam equivalent pressure of $3–4 \times 10^{-6}$ mbar. The InAs deposition takes place in a growth sequence of 0.1 ML InAs (at 0.06 ML/s) plus a 2 s pause under As flux. At the end of this sequence, the QDs are annealed 1 min to enhance the size distribution and to obtain medium density ensembles (10^9–10^{10} cm^{-2}). Subsequently, a thin GaAs cap layer is grown (at a rate of 1 ML/s) at different atmospheres and substrate temperatures, TCAP. In this way, QR are obtained under As_2 atmosphere at 1.1×10^{-6} mbar and TCAP = 500 °C, whereas other

[a] e-mail: jordi.gomis@uv.es

two different shape nanostructures are obtained by using As4 atmosphere, namely "quantum dashes" (QDh) at 1.6×10^{-6} mbar and TCAP = 540 °C, and "quantum camel-humps" (QC) are obtained at TCAP = 500 °C. The samples for Atomic Force Microscopy (AFM) characterization were cooled down immediately and removed from the growth chamber, while the samples for optical measurements were capped with a 50-nm-thick GaAs layer under a higher substrate temperature, 595 °C. More details of the sample growth and AFM characterization can be found on reference [5].

The nanostructure morphology was investigated by contact mode AFM (some micrographs are shown as insets in Fig. 1). The uncapped nanostructures called here QDh are elongated islands with typical length-width product around 160×40 nm^2, QC have the aspect of two camel-hump-like islands (around 100×50 nm^2 each "hump") and QR are similar to previous reported ring islands (100×90 nm^2) [4]. These nanostructures are characterized by smaller heights than their pyramidal InAs/GaAs counterparts. Uncapped quantum rings show typical heights around 1.5 nm, while QCs and QDh are slightly higher (2 nm).

It should be noted that the absolute dimensions given here are derived from the analysis of uncapped nanostructures. As found recently in cross-section high resolution transmission electron and scanning tunneling microscopy characterization of capped QRs, the uncapped values only remain approximately valid [7,8]. In addition, these studies also reveal a complicated composition profile resulting from the In/Ga exchange process taking place during the overgrowth step. These issues should be addressed below when discussing the optical and electronic properties of these samples. Continuous wave photoluminescence (PL) and excitation of the photoluminescence (PLE) of the samples were performed using a Ti:sapphire laser under low excitation densities with the sample held in an He-liquid immersion cryostat. The light was dispersed by a double 0.6 m focal length monochromator and synchronously detected by a Si-APD. The time resolved photoluminescence (TR-PL) as a function of the temperature (10–250 K), was dispersed by a single 0.5 m focal length imaging spectrometer and detected by a streak camera with a type S1 cooled photocathode. The overall time resolution in the widest temporal window (2 ns) was around 40 ps for excitation pulses of 2 ps pulsewidth at 76 MHz repetition rate. For this study, the sample was held on the cold finger of a closed-cycle cryostat.

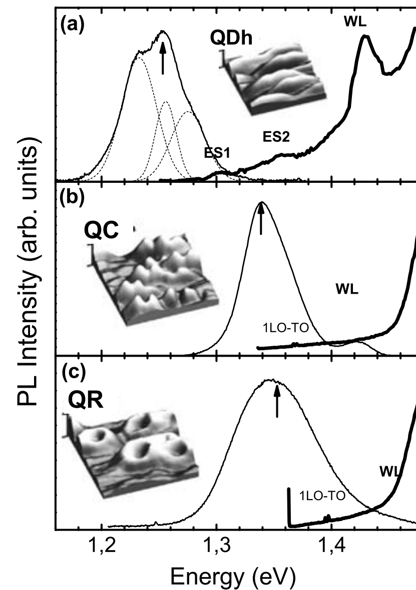

Fig. 1. PL (thin line) and PLE (thick line) spectra of (a) QDh, (b) QC and (c) QR ensembles. The arrows indicate the PLE detection energy. The first and second exited state (ES1 and ES2, respectively) and wetting layer (WL) resonances are indicated when observed.

3 Low temperature PL and PLE: origin of the emission

Figure 1 shows the PL spectra measured at low temperatures and using above barrier (GaAs) and low density excitation conditions. The ground state transitions are centered at 1.25, 1.34 and 1.35 eV for QDh, QC and QR nanostructures, respectively. As stated above, the ground optical transition energies for these kind of small nanostructures should mainly respond to the strong spatial confinement along the growth direction: QDh and QC are only 2 nm high, 3 to 5 times smaller than usual QD structures, and their ground states thus lie at higher energies than those, as expected. Nevertheless, despite their similar height, the QDh and QC emission bands are separated by an average energy difference of 90 meV, while the difference is negligible between QCs and QRs, whose heights estimated by AFM differ by roughly 2 MLs. This contradictory result clearly show that the particular In/Ga-alloying process leading to the formation of different shape nanostructures also leads to different composition profiles. This fact masks the simple and intuitive correlation between nanostructure size and confinement energy and makes difficult to compare our results with the electronic structure calculations reported for standard QDs in the literature.

The PL spectra shown in Figure 1 exhibit important size dispersion for the three samples, as revealed by the large full width at half maximum (FWHM): 60, 45 and 80 meV for QDh, QC and QR samples, respectively. The PL bands are approximately single Gaussians in the two latter cases, whereas three components can be nicely resolved for the sample containing QDh nanostructures as depicted by the three-Gaussian fit in Figure 1a. These three Gaussian components are peaked at 1.222, 1.250 and 1.274 eV and have linewidths below 30 meV. Given the low excitation conditions used here, a multi-modal behavior is assumed leading to three different QDh sub-ensembles whose average height would differ in 1 ML (two of the QDh families giving rise to two consecutive PL components split by 25 meV). With the given caution, such assignment is compatible with estimates for small lens shaped QD [9],

whose vertical dimensions are comparable to our nanostructures.

Figure 1 also shows the PLE spectra recorded for each sample. The PLE spectrum for the QDh sample reveals two resonances at around 55 meV and 110 meV above the detection energy, 1.250 eV. They must be related to the absorption at the *p*- and *d*-like excited state shells of the QDh family represented by that detection energy. When the PLE signal is detected on the low or high energy parts of the PL spectrum (namely, QDh families at 1.222 or 1.274 eV, respectively) we find similar values, consistent with an smooth change of the carrier confinement energy with the average QDh dimensions. We cannot observe any resolved contribution from excited state absorption in the PLE spectra of QC and QR ensembles, as observed in Figures 1b and 1c.

The continuum states contribution can be also investigated in the three samples. The WL related emission cannot be detected in the PL spectrum of the QDh sample (Fig. 1a). However, a well-resolved absorption line at 1.425 eV is associated to the WL exciton absorption peak in the corresponding PLE spectrum. On the contrary, the WL layer emission is observed clearly at around 1.44–1.45 eV for the QC ensemble, and also recognized in the high energy tail for the QR ensemble, but its corresponding absorption cannot be distinguished from the GaAs absorption edge in their PLE spectra (Figs. 1b and 1c). The differences found could indicate that the WL states are strongly (fast trapping times) correlated to the QDh carrier states thus producing strong PLE signal at the WL energy. Apparently, the relaxation is less efficient in the other two samples and the WL emission peak can be observed due to the dwelling time of the exciton in the continuum states.

More information can be obtained following the PL excitation density dependence for each sample. State filling of the *p*- and *d*-like excited state transitions can be observed for the QDh ensembles by increasing the pumping power, as observed in Figure 2a. We can identify contributions to the PL at around the aforementioned 55 and 110 meV above the ground state (the ground state emission and *p*–*d* excited states of the three QDh families are needed to obtain a reasonable multi-Gaussian fit to the experimental results). In the QC ensemble PL we find *p*- and *d*-like excited state recombination at around 35 and 68 meV above its ground state emission energy. This time only one Gaussian band is needed as shown in Figure 2b. Finally, we couldn't find any evidence of excited state recombination in the investigated QR sample, as shown in Figure 2c. A value around 40 meV for the energy splitting of the *s*–*s* and *p*–*p* exciton transitions has been found in similar samples with better size homogeneity, as reported in the literature [6,10–13]. This small value, as compared to the broad PL band representative of our QR ensemble (approximately 80 meV throughout the sample surface), makes the *p*-like emission unresolved on the high energy side of the measured PL spectra under high excitation density conditions. We finally should note that the splitting just found among the ground and excited shells are considerably smaller than the corresponding energies found in pyramidal InAs dots (70–100 meV). Again, with the caution given, this fact must be related with the larger lateral dimensions of our nanostructures compared with the latter.

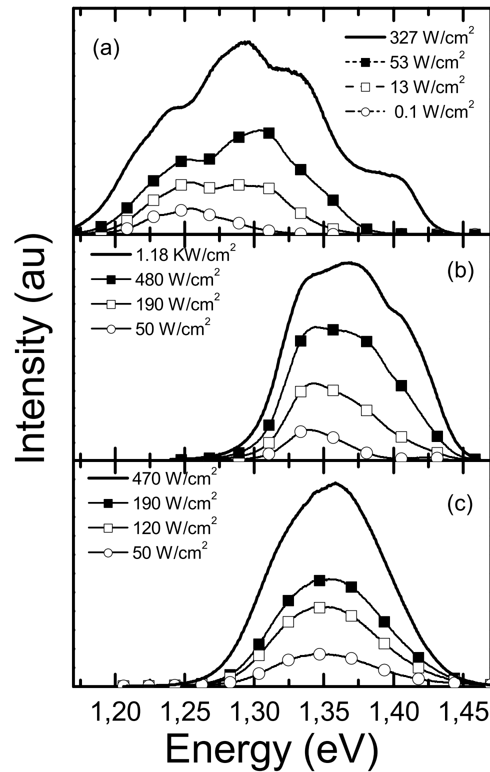

Fig. 2. PL at different excitation densities, as indicated inside each plot, for the different ensembles: (a) QDh, (b) QC and (c) QR.

4 Low temperature exciton lifetime

Figure 3 shows typical PL transients at 10 K for the three samples at the average PL peak energies. A fast rise time of the order of the experimental resolution is measured for the three types of ensembles and no phonon bottleneck is observed. The decay transient curves do not exhibit saturation effects at the relatively low powers used here. Nevertheless, we must note that we have not found significant changes of the PL decay time by increasing the excitation density by more than three orders of magnitude (after appropriate modeling of the saturation effects due to excited state filling).

Figure 4 summarizes the decay times measured under the same conditions as a function of the emission energy for the three samples. The PL decay time at the PL peak energy is typically larger for QDh nanostructures (850–950 ps) than for QC (750–800 ps) and QR (750–820 ps). The measured decay times are not very far from values found in literature for pyramidal InAs

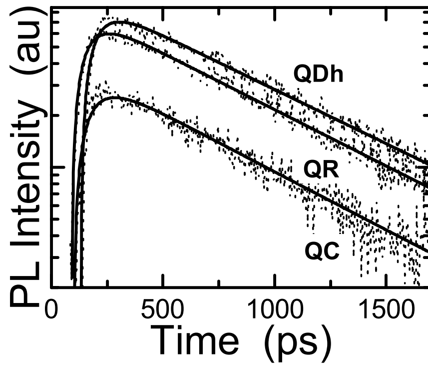

Fig. 3. PL transients measured at 10 K at the PL peak energy in the three samples under low excitation density conditions. The excitation wavelength was 765 nm.

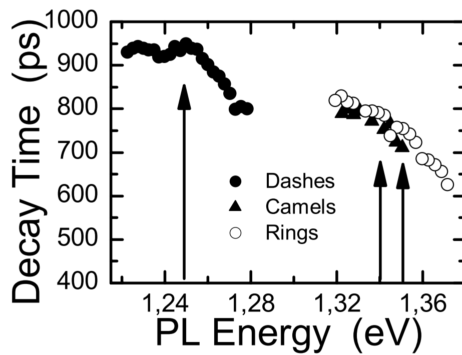

Fig. 4. PL decay time as a function of the detection energy under very low excitation densities for the different nanostructures.

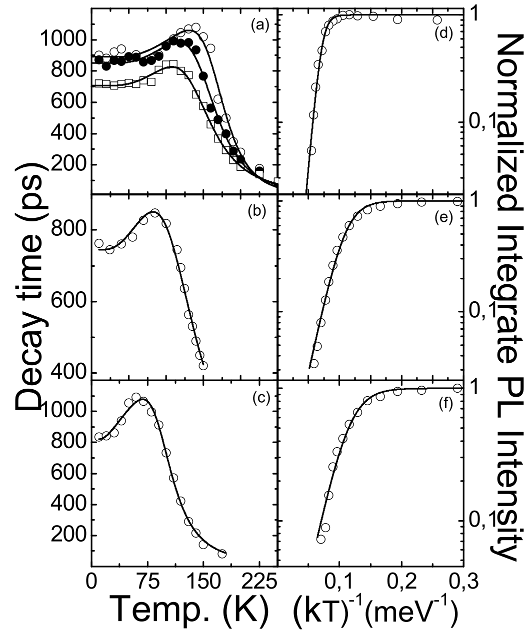

Fig. 5. PL decay time (left panel) and Arrenhius plot of the integrated PL intensity of the whole band (right panel) for QDh (a), QC (b) and QR (c) [(d), (e) and (f) at the right panel]. The evolution for the three QDh families resolved at 1.225 (hollow symbol), 1.250 (crossed symbol) and 1.274 eV (solid symbol) at low temperature are represented in (a). Continuous lines stand for the best fit to the experimental data obtained using equations (6) (right panel) and (12) (left panel).

dots [14,15], for which a certain dispersion of absolute values (within the range 1–2 ns) are found. Such a significant dispersion is usually attributed to different pyramidal truncation degree, which is giving rise to different oscillator strength of the ground state exciton optical transition [16].

If we only consider radiative mechanisms, due to the enhanced overlap among the electron and the hole wavefunctions, a shorter decay lifetime is expected for smaller QDs. As observed in Figure 4, our TRPL results exhibit such behavior and quantum confinement energy and decay lifetime are inversely correlated in the different samples. Also, for each sample, the decay time does not remain constant over the whole emission band: decreases on the high energy side of the PL bands, mainly above the average PL peak energies, as observed in Figure 4. Such a similar effect has been reported in pyramidal QD ensembles, and it must be attributed here to the increase of confinement by reducing the size volume of the nanostructure [17,18].

5 Radiative and non-radiative exciton dynamics

The temperature evolution of the integrated PL intensity and the ground state exciton lifetime (detection at the PL peak energy) are plotted in Figure 5. As observed, all samples are characterized by a similar behavior and two temperature regions can be defined in view of our results. In the first regime, the exciton recombination time increases with increasing temperature while the integrated intensity remains essentially constant. At a given temperature, the decay lifetime reaches its maximum and the second regime begins. Here, the exciton lifetime decreases monotonically with temperature while the PL band gets quenched. Above a given temperature, that depends on the carrier confinement energy, thermally activated carrier escape towards the continuum states is the main mechanism producing the observed PL intensity reduction [19–22]. Our nanostructures are capped only by GaAs barriers, therefore the carrier escape towards the wetting layer states opens the non radiative recombination channels at high temperatures: the corresponding non radiative recombination times should be comparable if not faster than the recapture time in the nanostructures [23]. However, the behavior at low temperatures deserves more attention. Its origin is attributed here to the thermal population of the first non-radiative excited state (electron in a *s*-like state and hole in a *p*-like state), competing with the exciton radiative recombination at the ground state (electrons and holes at *s*-like states) [22]. Emission and retrapping involving WL states [20] is discarded since we observe the same behavior over the entire PL band

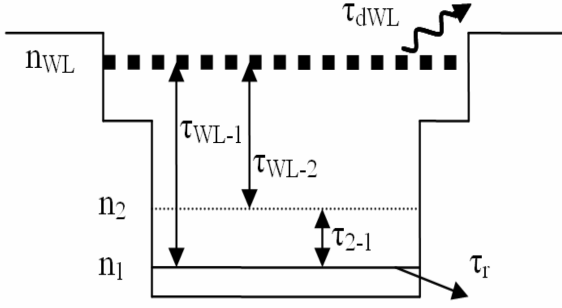

Fig. 6. Level distribution scheme in a simplified QD model.

(different dot sizes) and no carrier redistribution in the ensemble is observed.

The participation of s_e–p_h dark states in the thermalization process of the photogenerated excitons can be described as a two particle (uncorrelated) phenomenon. However, the capture and thermal escape of carriers does not take place independently for electrons and holes (unipolar escape), but involve Coulomb correlated electron-hole particles [24]. That is, a QD state occupied by an electron (hole) increases its probability to capture a hole (electron). Therefore, in order to model the temperature evolution by taking into account dark state thermalization, we develop a single particle (exciton) model similar to the one in reference [25] instead of a two particle model [26,27]. In the first case we will obtain an analytical expression, whereas the second leads to a system of coupled differential equations without analytical solution.

The energy level scheme representative of our model is depicted in Figure 6. The populations at ground, dark and WL (exciton) states are given by n_1, n_2, n_{WL}, respectively. The decay times for excitons at WL and ground states are labeled as τ_{dWL} and τ_r, respectively. The relaxation time from dark to ground state is τ_{2-1} and the exciton capture at n_1 and n_2 QD-levels from the WL states is represented by τ_{WL-1} and τ_{WL-2} times. The times for the opposite processes (up arrows in Fig. 6 indicating the particle transfer from low to high energy levels) can be found by assuming the system reaches a quasi-Fermi equilibrium without external excitations [28,29]:

$$\tau_{e2-1} = \frac{1}{g}\tau_{2-1}e^{\frac{\Delta E_{2-1}}{kT}} \quad (1)$$

$$\tau_{eWL-i} = \frac{1}{g'}\tau_{WL-i}e^{\frac{\Delta E_{WL-i}}{kT}} \quad (2)$$

where $\Delta E_{2-1} = E_2 - E_1$ is the energy difference between dark and ground states and $E_{WL-i} = E_{WL} - E_i$ the energy difference between the WL and the particular lower energy i-state (i = 1, 2). The g-factor accounts for the relative degeneracy between ground and dark states. The validity of the equations 1 was also discussed in reference [24] and attributed to the participation of phonon emission and absorption in the capture and escape processes, respectively. In a first approximation both kind of assumptions should depend on the degeneracy of the initial and final states involved in the relaxation process.

The level system (neglecting carrier recapture in the nanostructures) is then described by the following rate equation system:

$$\frac{dn_1}{dt} = -\frac{n_1}{\tau_r} - \frac{n_1}{\tau_{WL-1}}e^{-\frac{\Delta E_{WL-1}}{kT}} - \frac{n_1}{\tau_{2-1}}e^{-\frac{\Delta E_{2-1}}{kT}} + \frac{n_2}{\tau_{2-1}} + \frac{n_{WL}}{\tau_{WL-1}}, \quad (3)$$

$$\frac{dn_2}{dt} = \frac{n_1}{\tau_{2-1}}e^{-\frac{\Delta E_{2-1}}{kT}} - \frac{n_2}{\tau_{2-1}} - \frac{n_2}{\tau_{WL-2}}e^{-\frac{\Delta E_{WL-2}}{kT}} + \frac{n_{WL}}{\tau_{WL-2}}, \quad (4)$$

$$\frac{dn_{WL}}{dt} = G - \frac{n_{WL}}{\tau_{WL-1}} - \frac{n_{WL}}{\tau_{WL-2}} - \frac{n_{WL}}{\tau_{dWL}(T)}. \quad (5)$$

First of all we can calculate the integrated PL intensity evolution. Under steady state conditions thermal equilibrium is achieved and the PL intensity due to exciton recombination at the ground state can be obtained. Assuming $\tau_r \gg \tau_{2-1}$ and neglecting high order exponential terms we arrive to:

$$I_{PL}(T) = \frac{G \cdot p_{cQD}}{p_{cQD} + p_{eWL}(T)} \left(1 + \tau_r\left(\frac{1}{\tau_{WL-1}} + \frac{g}{\tau_{WL-2}}\right)e^{\frac{\Delta E_{WL-2}}{kT}}\right)^{-1} = \frac{I_{PL}(0)}{1 + B_{WL}e^{\frac{\Delta E_{WL-2}}{kT}}} \quad (6)$$

where $p_{cQD} = \frac{1}{\tau_{WL-1}} + \frac{1}{\tau_{WL-2}}$ and $p_{eWL} = \frac{1}{\tau_{dWL}(T)}$ are the QD capture rate from WL, and WL recombination rate (radiative and non radiative), respectively, and B_{WL} is proportional to the effective loss rate (inverse of the nonradiative recombination time) in the the WL.

By fitting the experimental data shown in Figures 5d–5f to equation (6), we- obtain the activation energies, E_{WL-1}, and the parameter B_{WL}, for each sample. In our samples, the exciton ground state lies not far from the WL states. Particularly, we have found E_{WL-1} around 150–175–200 meV for the three QDh families, and around 100 meV for QC-QR nanostructures, as was shown in Figure 1. At the same time, the WL states are also close to the bulk GaAs bandgap, around 90 meV in all samples. The PL quenching with increasing temperature is due to the thermal activation of excitons from confined states at the nanostuctures towards WL states, from where they are transferred towards the GaAs barriers. Once there the carriers will recombine non radiatively and recapture by WL and nanostructures is negligible, as assumed above. Due to the approximations made, the PL intensity evolution represented by 6 was independent of the dark state energy and the relaxation time (τ_{2-1}). However, the decay time evolution will be more sensible to the dark state contribution as discussed below. Firstly, we will assume a short excitation pulse writing for the gain function $G = \delta(t-t_0)$.

This way, we can integrate equation (5) alone to obtain:

$$n_{WL}(t) = C \cdot e^{-(p_{cQD}+p_{eWL}(T))t} \quad (7)$$

and showing that the WL population will vanish rapidly after pulsed excitation. At low temperatures, the exciton capture at nanostructures will produce a fast depletion of WL states. At high temperatures, their depletion will be produced by non radiative loses at the GaAs barrier, as discussed above. Therefore, at long times after pulsed excitation ($t \sim \tau_d$, where τ_d is the effective exciton recombination time), we can eliminate the WL contribution reducing the differential equation system only for ground and dark state populations, which can be solved by using initial conditions:

$$n_2(0,T) = 0;\; n_1(0,T) = e^{\frac{p_{cQD}}{(p_{cQD}+p_{eWL}(T))}}. \quad (8)$$

This it is not a strictly valid assumption, as the carriers should populate both ground and dark states right after pulsed excitation. However, as far as we are interested in the exciton population dynamics at long times after laser pulse($t \gg t_{2-1}$), if τ_{2-1} is short enough, we know that this system will arrive rapidly to equilibrium by thermalization of the n_1 and n_2 populations for a given temperature. The time evolution of the ground state population is thus given by:

$$n_1(t \gg \tau_{2-1}, T) = C \cdot e^{-\frac{t}{\tau_d(T)}} \quad (9)$$

where τ_d is obtained from the relevant constants entering in the exciton recombination dynamics:

$$\tau_d(T) = \frac{p_{cQD}}{p_{cQD}+p_{eWL}(T)} \frac{\tau_r\left(1+g\cdot e^{-\frac{\Delta E_{2-1}}{kT}}\right)}{1+\tau_r\left(\frac{1}{\tau_{WL-1}}+\frac{g}{\tau_{WL-2}}\right)e^{\frac{\Delta E_{WL-2}}{kT}}} = \frac{I_{PL}(T)}{g}\tau_r\left(1+g\cdot e^{-\frac{\Delta E_{2-1}}{kT}}\right) \quad (10)$$

and we have used $\tau_r \gg \tau_{2-1}$ and $e^{-\frac{\Delta E_{2-1}}{kT}} \gg e^{-\frac{\Delta E_{WL-1}}{kT}}$ in the studied temperature range.

The time decay constant given by equation (10) does not depend on τ_{2-1}, but it does strongly on the energy difference between the dark and ground states, E_{2-1}. Now, we can use equation (10) to fit the temperature evolution of the experimental PL decay time, as shown by continuous lines in Figures 5a–5c.

As we have seen, the parameter B_{WL} in equation (6) determined the PL intensity quenching and now also the time decay decrease, equation (10), at high temperatures. One could use the values of B_{WL} obtained from the steady state evolution shown in Figures 5d–5f to fit the whole temperature behavior of t_d. However, TRPL and PL experiments have inherent different excitation conditions making B_{WL} to be different in both cases, as was discussed in reference [24]. In our case, we also obtain different values for this constant in the fits of both PL and TRPL data to equations (6) and (5), respectively. It is also worth noting that small changes in the fitting parameters E_{WL-1} and E_{2-1} (within the error estimate) produce important changes in the value of B_{WL}. To reduce the degrees of freedom, we have fixed the parameter E_{WL-1} to be the same in both fitting sessions. The degeneracy relative factor g of the s_e–p_h dark exciton transition is also fixed as 2 [22]. Therefore, we only use as free fitting parameters E_{2-1} and B_{WL}, the first is determining the increase of t_d with temperature and the second is determining the decrease of t_d at high temperatures thus establishing the temperature at which takes place the maximum value of t_d in each sample (see Fig. 5).

Following this procedure we obtain for the QDh ensemble band: $E_{2-1} = 24.6 \pm 1.2$ meV for the lowest energy family, $E_{2-1} = 23.2 \pm 1.0$ meV for the middle energy family and $E_{2-1} = 20.7 \pm 1.0$ meV for the highest energy family. These energies are less than half the energy splitting between the p_e–p_h and s_e–s_h optical transitions found to be 55 meV in the previous sections. Within our model, they correspond to the energy separation among the p_h–s_e dark exciton with respect to the ground exciton in these nanostructures. For the other two samples, QC and QR, we find $E_{2-1} = 16.9 \pm 0.7$ eV and $E_{2-1} = 10.0 \pm 0.8$ meV (or 12.2 ± 0.96 and 6.2 ± 1.4 meV, if $g = 1$, which could be more appropriate if we think that circular symmetry is broken for lateral confinement in these nanostructures), respectively. The values found are consistent with reported values for hole confinement energies in small QDs. They also follow the expected evolution given the lateral dimensions found by AFM in each sample. As promised, the proposed rate equation model catches the evolution of the radiative and non-radiative exciton dynamics in the investigated temperature range. The thermalization between the ground and the first excited states dominates the intermediate temperature regime and is mediated by a thermally activated mechanism. At higher temperatures, carrier scape out of the nanostructures becomes important leading to a strong reduction of the exciton lifetime and the PL integrated intensity due to the non-radiative losses in the continuum states.

6 Conclusions

We have investigated InGaAs self-assembled nanostructures whose size and shape strongly depend on a single overgrowth step introduced during the self-assembling process. We have found that their electronic structure differs appreciably from typical QDs emitting at 1.1 eV. On the one hand, due to their smaller height, we observe an strong blue shift of the ground state energy. In spite of the strong energy shift, the three-dimensional confinement is still very efficient in these nanostructures and the radiative lifetime measured at low temperatures is below 1 ns in all cases, thus producing strong emission bands. The excited state structure has been also investigated and correlated with the exciton recombination dynamics at low and high temperatures. We observe an important increase

of the radiative lifetime with temperature, which is attributed to the thermalization between the ground radiative exciton state and the first excited dark state. A rate equation model has been developed to account for this exciton thermalization at intermediate temperatures and the non-radiative losses through WL states at high temperatures. The model reproduces our experimental data and gives insight in the exciton recombination dynamics in this system which should be taken into account in the future devices design.

This work has been supported by the Spanish Nanoself I and II projects TIC2002-04096-C03 and TEC2005-05781-C03-03, Generalitat Valenciana and SANDiE Network of excellence (Contract number NMP4-CT-2004-500101 group TEP-0120).

References

1. D. Bimberg, J. Phys. D: Appl. Phys. **38**, 2055 (2005)
2. K. Ouchi, T. Mishina, J. Cryst. Growth **209**, 242 (2000)
3. J.M. Ripalda, D. Granados, Y. González, A.M. Sánchez, S.I. Molina, J.M. García, Appl. Phys. Lett. **87**, 202108 (2005)
4. J.M. García, G. Medeiros-Ribeiro, K. Schmidt, T. Ngo, P.M. Petroff, Appl. Phys. Lett. **71**, 2014 (1997)
5. D. Granados, J.M. García, Appl. Phys. Lett. **82**, 2401 (2003)
6. R. Warburton, C. Schaflein, D. Haft, F. Bickel, A. Lorke, K. Karrai, J. García, W. Schoenfeld, P. Petroff, Nature **405**, 926 (2000)
7. P. Offermans, P.M. Koenraad, J.H. Wolter, D. Granados, J.M. García, V.M. Fomin, V.N. Gladilin, J.T. Devreese, Appl. Phys. Lett. **87**, 131902 (2005)
8. D. Granados, J.M. García, T. Ben, S.I. Molina, Appl. Phys. Lett. **86**, 071918 (2005)
9. F. Guffarth, R. Heitz, A. Schliwa, K. Potschke, D. Bimberg, Physica E **21**, 326 (2004)
10. H. Pettersson, R. Warburton, A. Lorke, K. Karrai, J. Kotthaus, J. García, P. Petroff, Physica E **6**, 510 (2000)
11. A. Lorke, R. Luyken, A. Govorov, J. Kotthaus, J. García, P. Petroff, Phys. Rev. Lett. **84**, 2223 (2000)
12. B. Alén, J. Martínez-Pastor, D. Granados, J. García, Phys. Rev. B **72**, 155331 (2005)
13. D. Haft, C. Schulhauser, A. Govorov, R. Warburton, K. Karrai, J. García, W. Schoenfeld, P. Petroff, Physica E **13**, 165 (2002)
14. R. Heitz, A. Kalburge, Q. Xie, M. Grundmann, P. Chen, A. Hoffmann, A. Madhukar, D. Bimberg, Phys. Rev. B **57**, 9050 (1998)
15. C. Santori, G. Solomon, M. Pelton, Y. Yamamoto, Phys. Rev. B **65**, 073310 (2002)
16. R. Heitz, H. Born, F. Guffarth, O. Stier, A. Schliwa, A. Hoffmann, D. Bimberg, Phys. Stat. Sol. (a) **190**, 499 (2002)
17. J. Bellessa, V. Voliotis, R. Grousson, X. Wang, M. Ogura, H. Matsuhata, Phys. Rev. B **58**, 9933 (1998)
18. M. Sugawara, Phys. Rev. B **51**, 10743 (1995)
19. H. Yu, S. Lycett, C. Roberts, R. Murray, Appl. Phys. Lett. **69**, 4087 (1996)
20. W. Yang, R. Lowe-Webb, H. Lee, P. Sercel, Phys. Rev. B **56**, 13314 (1997)
21. A. Fiore, P. Borri, W. Langbein, J. Hvam, U. Oesterle, R. Houdré, R. Stanley, M. Ilegems, Appl. Phys. Lett. **76**, 3430 (2000)
22. M. Gurioli, A. Vinattieri, M. Zamfirescu, M. Colocci, S. Sanguinetti, R. Nötzel, Phys. Rev. B **73**, 085302 (2006)
23. G. Bacher, C. Hartmann, H. Schweizer, T. Held, G. Mahler, H. Nickel, Phys. Rev. B **47**, 9545 (1993)
24. E.L. Ru, J. Fack, R. Murray, Phys. Rev. B **67**, 245318 (2003)
25. S. Sanguinetti, M. Henini, M.G. Alessi, M. Capizzi, P. Frigeri, S. Franchi, Phys. Rev. B **60**, 8276 (1999)
26. T. Norris, K. Kim, J. Urayama, Z. Wu, J. Singh, P.K. Bhattacharya, J Phys D: Appl. Phys. **38**, 2077 (2005)
27. P. Dawson, O. Rubel, S. Baranovskii, K. Pierz, P. Thomas, E.O. Göbel, Phys. Rev. B **72**, 235301 (2005)
28. A. Markus, A. Fiore, Phys. Stat. Sol. (a) **201**, 338 (2004)
29. H. Jiang, J. Singh, J. Appl. Phys. **85**, 7438 (1999)